DOI: 10.21062/mft.2024.062 http://www.journalmt.com

Microstructural Analysis, Corrosion Resistance, and Wear Performance Study of $Al_{0.8}FeCoNiCrCu_{0.5}Si_{0.2}$ High-Entropy Alloy

Peng Zhang (0009-0003-1570-8706), Yanzhou Li (0009-0007-7762-4355)*
School of Mechanical and Vehicle Engineering, West Anhui University, Lu'an 237012, Anhui, China.
E-mail: liyanzhou9336@163.com (corresponding author)*, 04000141@wxc.edu.cn

The high-entropy alloy with the composition Al0.8FeCoNiCrCu0.5Si0.2 was produced through a process in-volving a vacuum arc melting method. Comprehensive characterization was performed through techniques such as XRD, SEM, and TEM. The findings revealed that the alloy primarily consists of Fe-Cr and Al-Ni phases, displaying predominantly two body-centered cubic structures. The alloy exhibited a characteristic dendritic cast structure. The alloy predominantly has high-angle grain boundaries accounting for 96.1%. Its grains demonstrate minimal internal strain and reduced lattice anomalies. The alloy showcased resistance with a corrosion current density of 1.4×10-7 A/cm2 and a corrosion potential of 0.28047 V. Post-corrosion examinations emphasized regions abundant in Al and Cu as the primary degradation sites. The addition of Si has further improved the alloy's resistance to corrosion. In terms of abrasion durability, the alloy exhibit-ed a wear scar length of only 1.42 mm, substantially less than the 1.88 mm found in 45 carbon steel, highlighting its enhanced resistance to wear. This wear resistance is attributed to its inherent BCC1 and BCC2 phase structures and the hardness it derives from its unique composition. Owing to its superior traits, this high-entropy alloy presents promising potential for applications, including coatings, and advanced automotive components.

Keywords: $Al_{0.8}FeCoNiCrCu_{0.5}Si_{0.2}$, Microstructure, Corrosion resistance, Wear resistance

1 Introduction

High-entropy alloys (HEAs) are increasingly a focus in contemporary materials science, noted for their innovative alloy composition and remarkable characteristics [1-6]. It deviates from the traditional alloy approach centered around a single principal element and mixing enthalpy. This new class of metallic materials, featuring multiple principal elements, is innovatively designed with a primary focus on configurational entropy [7]. The diverse elemental composition of HEAs enhances the system's mixing entropy, lowering the Gibbs free energy [8-11]. Due to these outstanding performance characteristics, HEAs are emerging as materials with significant potential in the field of surface engineering [12-18]. To date, the preparation methods for HEAs chiefly include vacuum arc melting (VAC)[19, 20] and powder metallurgy[21, 22]. Among these, VAC is particularly notable as it effectively removes gases and impurities during the melting process, making it a widely adopted method. In this study, the $Al_{0.8}FeCoNiCrCu_{0.5}Si_{0.2}$ HEA was synthesized using VAC.

Earlier studies on transition metal high-entropy alloys predominantly focused on two main systems: the BCC structure of the AlFeNiCoCr system and the BCC structure of the AlFeNiCoCr system. Alloys such as CoCrFeMnNi in the FCC phase display noteworthy ductility, achieving a room-temperature elongation of 52%, and their tensile strength tops out at 563 MPa [23]. The $Fe_{40}Mn_{40}Co_{10}Cr_{10}$ alloy, while reaching an elongation of 58%, presents a rather reserved yield strength at a mere 240 MPa [24]. Single-phase BCC alloys have exhibited high hardness [25].In recent years, the research has mainly centered on introducing various reinforcement mechanisms to balance the alloy's strength and ductility. For instance, the introduction of high-density twins or grains into the alloy through cold rolling and annealing processes leads to grain boundary strengthening [26]. By aging treatment of supersaturated alloys, the formation of nano-scaled L12 phase can be achieved, leading to coherency strengthening [27]. By adjusting the alloy components, hard and brittle BCC/B2 phases can be introduced into FCC phase alloys, resulting in non-coherent secondary phase strengthening [28]. Through thermomechanical treatments, multi-scale heterogeneous structures can be induced in the material, leading to heterogeneous structure strengthening [29]. These distinctive structures and reinforcing phases in high-entropy alloys can be realized through straightforward adjustments in composition and thermomechanical processing. This approach facilitates the discovery of alloys that are both high in strength and ductility. In terms of adding elements to improve alloy performance, principal elements such as Cu, Ti, and Mo can be incorporated.

Studies have indicated that introducing a secondary phase in high-entropy alloys (HEAs) is an effective approach to enhancing their comprehensive mechanical properties. For instance, carbon has shown a positive impact on CoCrFeMnNi[30], CoCrFeNi[31], and AlCoCrNiTi[32] HEAs. Carbon in these alloys leads to solid solutions or carbides, increasing both hardness and fracture toughness through strengthening. Similarly, elements like boron (B) and silicon (Si), when forming interstitial solid solutions or secondary phases with metals, can also elevate the strength of HEAs. Introducing boron into FeCoCrNi HEAs resulted in the creation of FCC and borides. Although these borides improved hardness and strength, they also caused a minor reduction in ductility and elongation [33]. Xu et al. [34] investigated characteristics of $VNbTiTaSi_x$ HEAs, finding that the presence of M_5Si_3-type silicides emerged when Si content reached 2.5 and 5 mass%; whereas, when Si content rose to 10 mass %, the alloy was primarily composed of M_5Si_3 and M_3Si. Xin et al. [35] discerned that silicon could amplify the hardness of $Al_{0.2}Co_{1.5}CrFeNi_{1.5}Ti_{0.5}$ HEAs. Thus, adjusting non-metallic elements and microstructure in high-entropy alloys can potentially improve their mechanical properties.

Our prior work has identified that the $Al_{0.8}CrFeCoNiCu_{0.5}$ HEA formed three distinct phase structures - BCC1, BCC2, and FCC, showcasing moderate corrosion resistance [36]. The segregation of copper at grain boundaries negatively impacted its corrosion-resistant characteristics. This study primarily focuses on the $Al_{0.8}FeCoNiCrCu_{0.5}Si_{0.2}$ HEA, aiming to elucidate its microstructural attributes along with wear and corrosion resistance. To shed light on silicon's role within HEAs and its influence on copper segregation, further elucidating how this interplay shapes the corrosion resistance mechanism of the alloy. This research offers pivotal theoretical insights for the AlCoCrFeNiCu HEA system and holds significant practical engineering implications.

2 Materials and Methods

In this study, an X-DHL400 non-consumable vacuum arc melting furnace was harnessed to create $Al_{0.8}FeCoNiCrCu_{0.5}Si_{0.2}$ alloy samples. Each element used had a minimum purity of 99.95%. The alloy was created in a vacuum furnace under argon gas, using titanium blocks to remove contaminants before melting. Each sample was melted five times for elemental uniformity. The midsections were cut for microstructure and performance analysis.

The samples were polished to a reflective finish and etched with a 2:6:8 mix of HNO3, HCl, and ethanol for microstructure exposure. A two-step polishing, mechanical and then electrochemical in a 10% ethanol and chloric acid solution was performed for 30 seconds.

The alloy's crystal structure was analyzed using a Shimadzu XRD7000S X-ray diffractometer from Japan, with a Cu Kα radiation source of wavelength 0.154056nm. The operating conditions were set at 40kV and 40mA. The alloy's microstructure was studied with Hitachi's SU6600 SEM and Oxford's UltimMax100 EDS for elemental analysis. Grain morphology and orientation were analyzed through EBSD using the Oxford Symmetry module, operating at 20kV with a 5.6 nA current and 0.5μm scanning increment. Data analysis was conducted via the Aztec platform. The JEM-2010 TEM was employed for detailed crystallography studies.

The electrochemical analysis used the Nova2 platform from Metrohm, Switzerland, for potentiodynamic polarization and electrochemical impedance spectra measurement. Data analysis was facilitated by ZView software. Utilizing the MM-10000A tester, the alloy's wear resistance was evaluated through a dry sliding test, enduring a sustained 200 N pressure for 20 minutes. Before the assessment, the specimen was meticulously refined with fine-grit sandpaper, ensuring a smooth surface, and underwent an ultrasonic cleanse in an ethanol solution, a process replicated post-experiment.

3 Results and discussion

3.1 XRD analysis

Fig. 1 depicts the XRD of the $Al_{0.8}FeCoNiCrCu_{0.5}Si_{0.2}$ HEA. The diffraction patterns corresponding to the BCC1 phase. Diffraction peaks associated with the BCC1 phase, matching the <110> and <200> crystallographic planes, emerge around 44.8° and 65°, a characteristic of the Fe-Cr phase. A distinct peak at 31.3° indicates the existence of BCC2, aligning with the Al-Ni phase on the <100> plane [37]. No evidence of intermetallic compounds with Si suggests that the added Si is incorporated in the alloy either as a solid solution or in its primary form. This supports the premise that non-metallic elements can partake in high-entropy phase formation with transition metals, in line with previous research on the as-clad $Al_{0.8}FeCoNiCrCu_{0.5}Si_{0.2}$ alloy [38]. Compared to $Al_{0.8}FeCoNiCrCu_{0.5}$ alloy, the FCC phase was not observed [39].

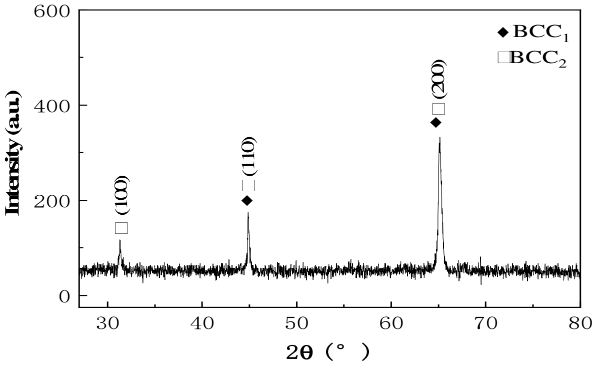

Fig. 1 *XRD of $Al_{0.8}CrFeCoNiCu_{0.5}Si_{0.2}$*

Fig. 2 predictions for the $Al_{0.8}CrFeCoNiCu_{0.5}Si_{0.2}$ HEA were conducted with ThermoCalc (v. 2022a) and the TCHEA6 database. The resulting equilibrium phase diagram, depicted in Figure 2, shows the alloy primarily solidifying in the BCC phase, with liquid and solid phase temperatures at 1353℃ and 1271℃, respectively. The FCC phase starts forming around 1224℃, increasing in volume as temperature decreases. At 1219℃, the BCC2 phase appears. These results indicate the possible coexistence of BCC1, BCC2, and FCC. In line with experimental findings, the alloy predominantly shows BCC1 and BCC2 phases.

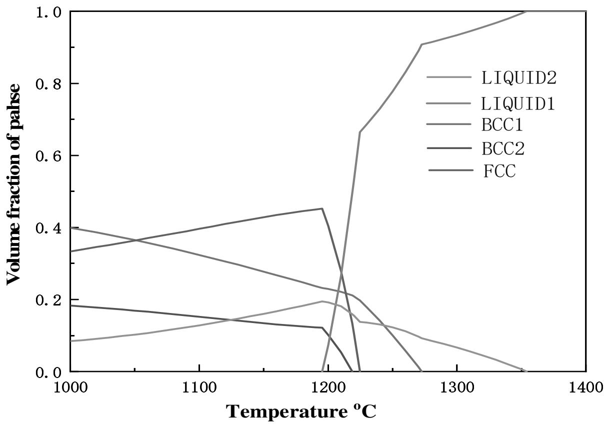

Fig. 2 *Phase diagram calculation of $Al_{0.8}FeCoNiCrCu_{0.5}Si_{0.2}$ HEA*

The Gibbs free energy formula, ΔGmix = ΔHmix – TΔSmix, implies that in alloys with many components of similar atomic percentages, ΔSmix is significantly increased, thereby reducing the system's ΔGmix. This reduction discourages the formation of ordered intermetallic compounds and enhances element solubility, promoting a random atom distribution within the lattice and resulting in a disordered solid solution. Therefore, this alloy exhibits fewer phases than those anticipated by the Gibbs phase rule.

Additionally, the slight variations in mixing enthalpy and atomic size among elements such as Cr, Co, Ni, and Fe, facilitate atomic substitutions in the lattice, promoting the formation of solid solutions. The comparable valence electron concentrations of these elements result in similar chemical bonding within the lattice, simplifying substitutions and further fostering the formation of solid solutions. This similarity also means a more even valence electron distribution in the alloy lattice, which minimizes energy fluctuations, thereby increasing the alloy's stability and the likelihood of forming a solid solution.

3.2 Microstructure

Fig. 3 showcases the unetched surface and corresponding scanning imagery of the $Al_{0.8}FeCoNiCrCu_{0.5}Si_{0.2}$ HEA. Tab. 1 details the elemental distribution data. The post-melting alloy composition closely matches the expected theoretical values.

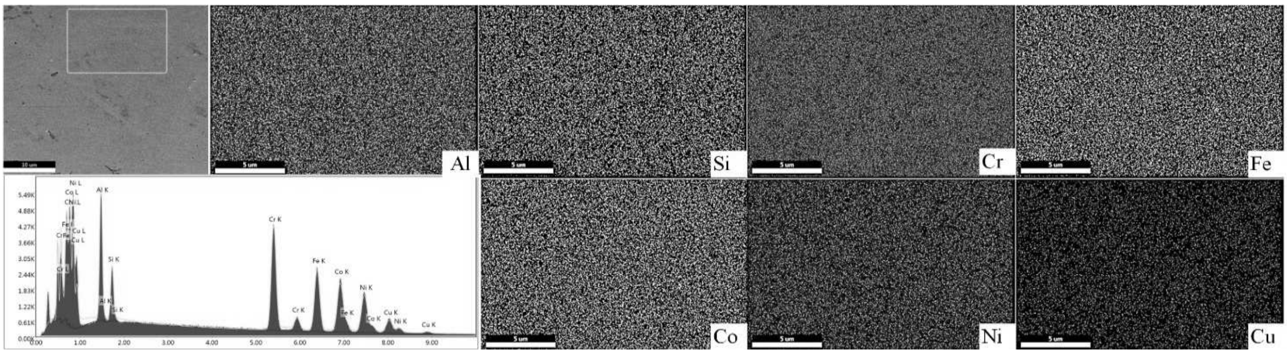

Fig. 3 *Surface Texture and Related Scanning Results of the $A_{l0.8}FeCoNiCrCu_{0.5}Si_{0.2}$ HEA*

Tab. 1 *Elemental Distribution in Al0.8FeCoNiCrCu0.5Si0.2 HEA, Corresponding to Figure 3*

Element	Al	Cr	Fe	Co	Ni	Cu	Si
Atomic %	13.80	21.46	18.36	17.41	17.12	7.29	4.85

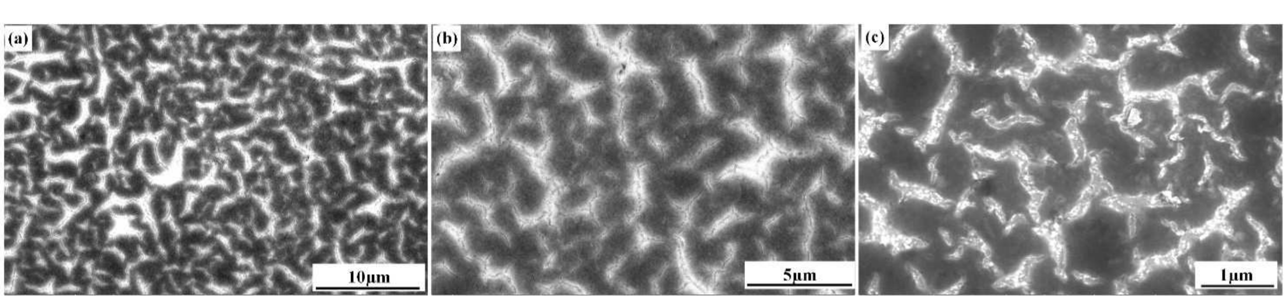

Fig. 4 *The SEM of $Al_{0.8}FeCoNiCrCu_{0.5}Si_{0.2}$ HEA at various magnifications: (a) 5000× (b) 10000× (c) 35000×*

Fig. 4 depict the microstructural SEM images of the $Al_{0.8}CrFeCoNiCu_{0.5}Si_{0.2}$ HEA after aqua regia etching at different magnifications. The alloy exhibits a characteristic dendritic cast structure.

EBSD analysis further explored the microstructure of the alloy. Fig. 5a displays the grain boundary and Kernel Average Misorientation maps. KAM, associated with dislocation density, reflects residual strain in grains, with significant strain observed mainly at grain boundaries and minimal internal strain in grains, indicating reduced lattice anomalies. The map utilizes red and black lines to indicate grain boundaries with low angular deviation, ranging from 2° to 15°, and grain boundaries with high angular deviation, having angles greater than 15°.The presence of 3.88% low-angle and 96.1% high-angle grain boundaries points to minimal residual stress in the alloy. Figure 5b illustrates the alloy's phase, confirming the primary presence of a red BCC phase, in agreement with XRD results. Fig. 5c provides a view of the random grain orientation, as indicated by the inverse pole figure.

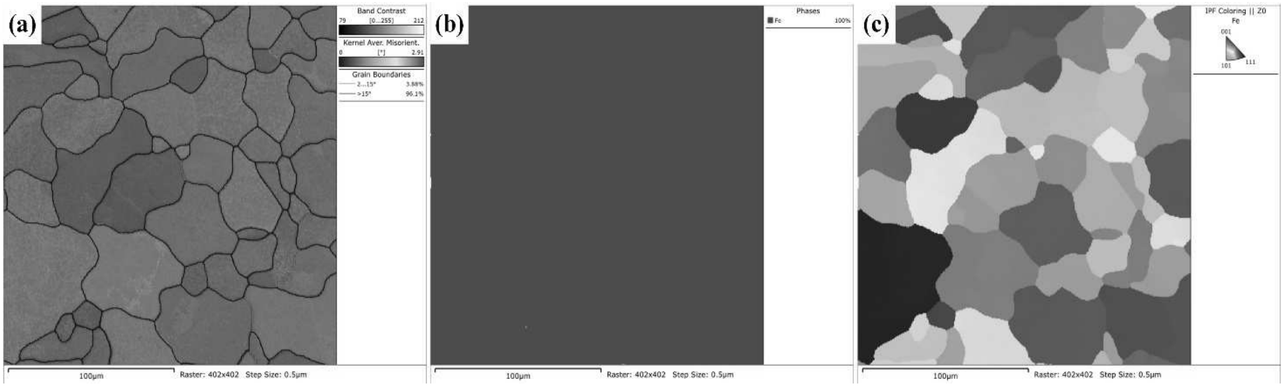

***Fig. 5** The EBSD of the $Al_{0.8}FeCoNiCrCu_{0.5}Si_{0.2}$ (a) BC+KAM map (b) phase map, (c) EBSD BC+IPFmap*

Fig. 6 displays TEM analysis of $Al_{0.8}FeCoNiCrCu_{0.5}Si_{0.2}$ HEA. In Figure 6(a), a low-magnification TEM bright field image reveals the grain and grain boundary morphologies, with two distinct grain types labeled Grain 1 and Grain 2.

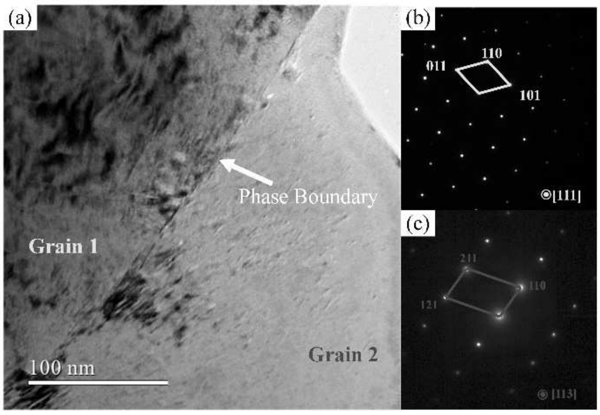

***Fig. 6** TEM of the $Al_{0.8}FeCoNiCrCu_{0.5}Si_{0.2}$ HEA (a) Bright field image (b) (c) SEAD*

Selected area electron diffraction for these grains, as shown in Figures 6(b) and 6(c), confirms the presence of the BCC phase, consistent with XRD and EBSD observations. Contrasting the behavior in the AlFeCoNiCrCu HEA, the distribution of the AlNi phase within the grains appears irregular, lacking the periodic patterns often attributed to spinodal decomposition [40]. This suggests that the AlNi phase might have precipitated within the grains through a continuous decomposition mechanism.

3.3 Corroison resistance

Electrochemical tests were employed to assess the corrosion resistance of the sample according to the standard ASTM-G3-89. Fig. 7a displays the dynamic potential polarization curves, from which the trend of the sample's polarization curve is visible. The sample shows a low Icorr of 1.4×10-7 A/cm2 and a positive Ecorr of 0.28047 V, a notable improvement over the earlier Al0.8FeCoNiCrCu0.5with an Icorr of 2.61×10-6 A/cm2 [36]. According to electrochemical theory, materials with superior corrosion resistance should exhibit lower values of both Icorr and positive E_{corr}. The incorporation of Si evidently enhances the alloy's resistance to corrosion. In comparison with Fig. 7b, it can be concluded that the corrosion occurring on the sample surface is pitting corrosion.

Fig. 8 reveals the corroded surface of the alloy, showing clear signs of corrosion products and pits. The distribution of Cr, Ni, Co, and Fe elements show similar patterns and are noticeably absent in areas where corrosion products form, suggesting their minimal involvement in the development of these products. In contrast, the compositional maps for Cu and Al demonstrate a lack of these elements at the sites of corrosion pits, pointing to significant corrosion in Al and Cu-rich areas during polarization. The presence of Al and Cu at the corrosion sites confirms their role in the corrosion process, leading to the formation of corrosion products on the alloy's surface. EIS was used to better understand the corrosion behavior of $Al_{0.8}FeCoNiCrCu_{0.5}Si_{0.2}$ HEA.

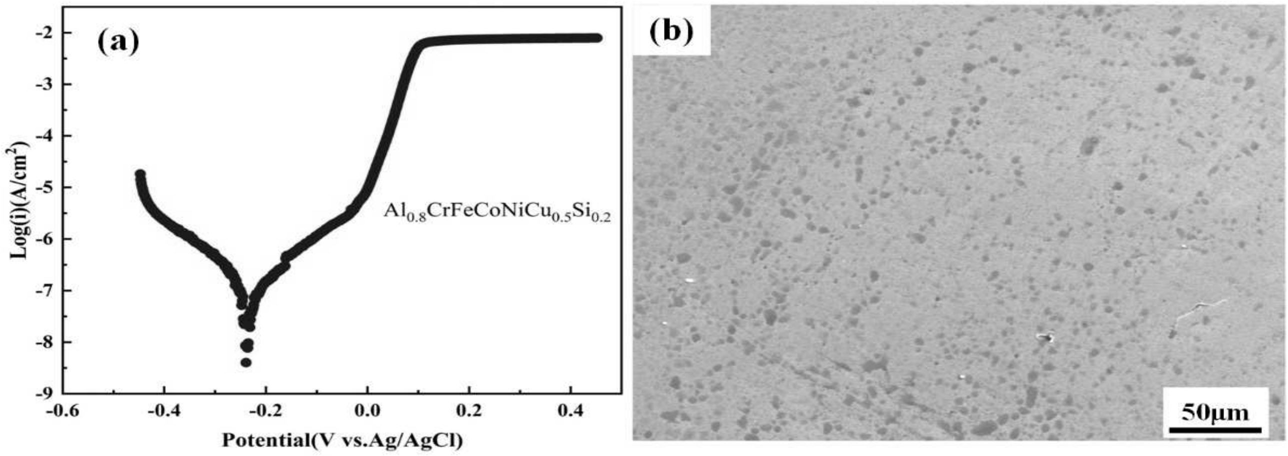

Fig. 7 *The polarization curve of Al0.8FeCoNiCrCu0.5Si0.2 HEA*

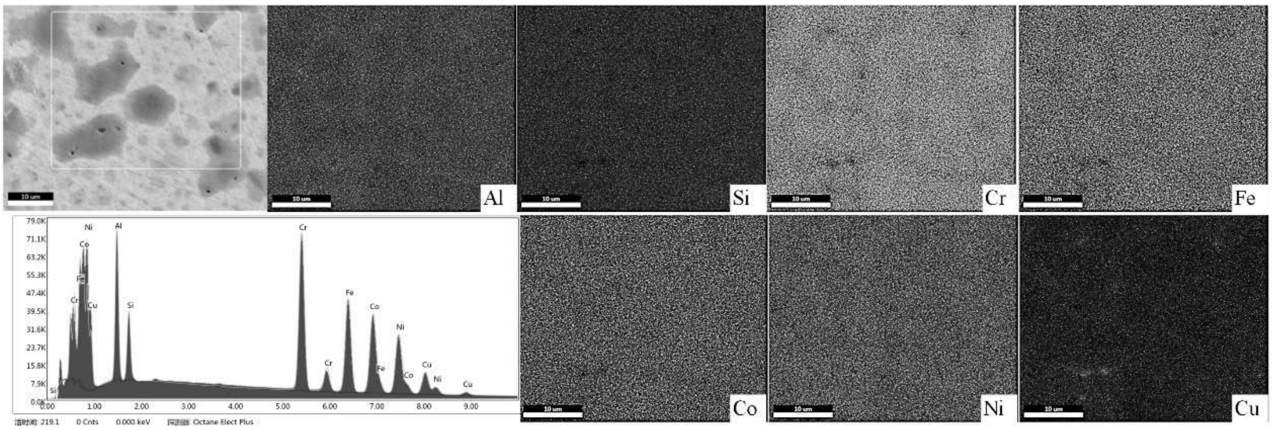

Fig. 8 *Corrosion patterns and targeted surface composition analysis of the $Al_{0.8}FeCoNiCrCu_{0.5}Si_{0.2}$ alloy*

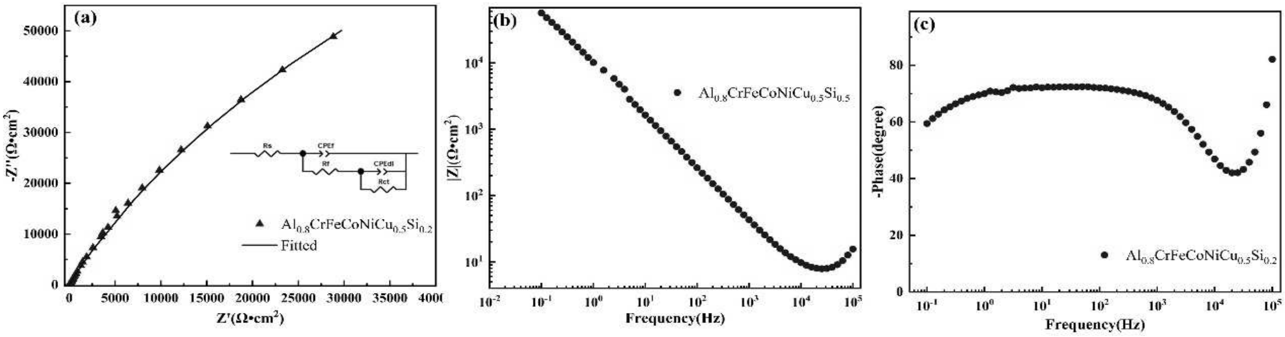

Fig. 9 *The EIS of the Al0.8FeCoNiCrCu0.5Si0.2 HEA. (a) Nyquist plot (b) Bode plot (c) Phase angle*

Fig. 9 further assesses corrosion resistance of sample by showcasing the Nyquist plots, impedance modulus curves, and phase angle diagrams of the in a 3.5 wt% sodium chloride solution. The Nyquist plot features scatter points for actual data and a connected curve for fitted data. In the impedance plot, the capacitive semicircle's diameter reflects the alloy's resistance to corrosion, where a bigger diameter signifies better corrosion protection. The impedance curve predominantly exhibits a capacitive arc, indicative of robust capacitive behavior. In these plots, the high-frequency region often corresponds to the properties of the surface passivation film.

In the analysis, the low-frequency zone reveals information about the region beneath the passivation film, suggesting that long-term corrosion can penetrate the cladding material. In the Bode plot, a greater magnitude of impedance (|Z|) is indicative of enhanced corrosion resistance [41]. Figure 8b reveals that the sample's |Z| value hits 56710.8Ω·cm² in the low-frequency phase. High phase angles at high frequencies and substantial moduli at low frequencies both signal robust corrosion resistance. The sample maintains high phase angles across various frequencies, underscoring its superior corrosion resistance.

The analysis of AC impedance spectra is generally conducted via equivalent circuits, which essentially consist of pure resistances R and pure capacitances C, with an impedance value of 1/jwC[42]. In the electrochemical characteristics of the sample, Rs signifies the solution resistance. This value, at 4.68Ω·cm2, signifies the impedance to charge transfer in the aqueous setting. Rf indicates the sample's surface resistance, measuring its capability to hinder corrosive ions from penetrating the interior, recorded at 12.35Ω·cm^2. Rct signifies the resistance to charge transfer at the sample surface, indicating its effectiveness in obstructing interfacial charge movement, measured at 303930Ω·cm^2. This implies significant resistance to corrosive ions entering the sample. CPE replaces the pure capacitor in the equivalent circuit [43]. The CPE is a non-ideal capacitor set for circuit fitting, which performs better in the equivalent circuit than a pure capacitor [44]. CEFf denotes the constant phase element linked to the double layer on the sample's exterior, reflecting the charge holding ability in this stratum [45]. CEFdl is the constant phase element situated at the interface between the film and the substrate, signifying its capacity to prevent ion diffusion at this boundary.

The polarization tests and impedance spectrum results indicate that its corrosion resistance surpasses that of $Al_{0.8}FeCoNiCrCu_{0.5}Si_{0.2}$ HEA, suggesting that the addition of Si enhances the alloy's anti-corrosion properties. Combined with microstructural analysis results, it can be inferred that Si inhibits Cu segregation, thereby boosting the alloy's corrosion resistance.

3.4 Wear resistance

Fig. 10 provide the wear morphologies of 45# steel and $Al_{0.8}FeCoNiCrCu_{0.5}$ $Si_{0.2}$ HEA, respectively. The comparison reveals a wear scar length of 1.88 mm for 45 carbon stell, whereas that of the $Al_{0.8}FeCoNiCrCu_{0.5}$ $Si_{0.2}$ HEA, is only 1.42 mm. This observation confirms the HEA's exceptional wear resistance when compared to 45# steel.

Fig. 10c and Fig. 10d present the three-dimensional laser scanning microscopy images of wear scars on the surfaces of both 45 carbon steel and the high-entropy alloy. The wear scar on the steel surface is visibly broader compared to the high-entropy alloy. The widened scar on the steel indicates a larger real contact area during friction, suggesting significant wear of the steel against the counterface [46]. In contrast, the high-entropy alloy's surface is smoother, with finer surface undulations revealing densely and smoothly arranged plow grooves within the wear scar. Such observations underline the enhanced wear resistance of HEA compared to 45# steel.

Fig. 11 illustrates the wear patterns of 45# steel and HEA. The 45# steel surface, as seen in Fig. 10a, shows significant plastic deformation. In contrast, Fig. 10b reveals the wear morphology of the HEA, where a detailed examination reveals both adhesive and abrasive wear, indicating these as the primary wear mechanisms. The alloy, primarily composed of BCC1 and BCC2 phases, demonstrates substantial lattice distortion and increased hardness due to its rich elemental composition [47].

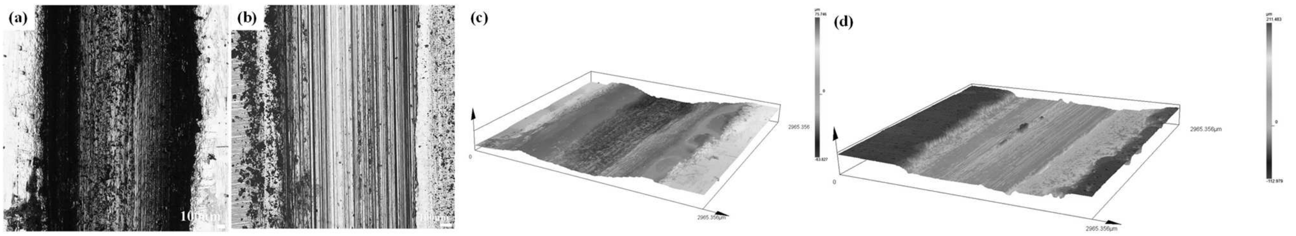

Fig. 10 *The wear test result and 3D laser measurement microscope photos (a)(c) 45# wear scar (b)(d) HEA*

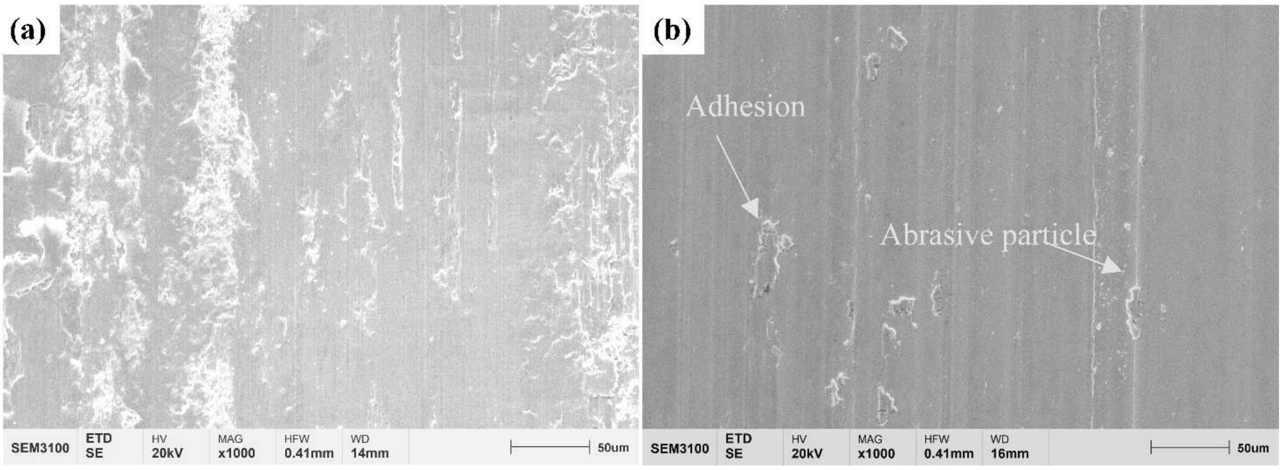

Fig. 11 *Wear morphology of the sample (a) 45# steel (b)* $Al_{0.8}CrFeCoNiCu_{0.5}Si_{0.2}$*HEA*

4 Conclusion

The findings from this study on the $Al_{0.8}FeCoNiCrCu_{0.5}Si_{0.2}$ HEA emphasize its notable wear resistance and corrosion properties. Main Conclusions:

- (1) The $Al_{0.8}FeCoNiCrCu_{0.5}Si_{0.2}$ HEA mainly showcases BCC1 and BCC2 phases, with BCC1 corresponding to (Fe-Cr) compositions and BCC2 associated with Al-Ni compositions. Additionally, the introduction of Si mitigates Cu segregation.
- (2) The $Al_{0.8}FeCoNiCrCu_{0.5}Si_{0.2}$ HEA showcased a dendritic cast structure. A majority of its grain boundaries were high angle, amounting to 96.1%, with minimal internal residual strains, indicating limited lattice defects.
- (3) The $Al_{0.8}FeCoNiCrCu_{0.5}Si_{0.2}$ HEA demonstrated notable corrosion resistance, with a low I_{corr} of 1.4×10^{-7} A/cm^2 and a positive I_{corr} of 0.28047 V. The addition of Si has further improved the alloy's resistance to corrosion. Pitting corrosion emerged as the predominant corrosion mechanism. Surface examinations post-corrosion highlighted regions rich in Al and Cu as primary areas of degradation.
- (4) The $Al_{0.8}FeCoNiCrCu_{0.5}Si_{0.2}$ high-entropy alloy exhibited a wear scar length of 1.42 mm, compared to the 1.88 mm in 45# steel. The primary wear mechanisms on HEA were adhesive and abrasive wear, with its enhanced wear resistance attributed to its BCC1 and BCC2 phase structures and inherent hardness from its composition.

Acknowledgement

This study was supported by the High-level Talents Research Project of West Anhui University (Grant No. WGKQ2021068), the Opening Project of Key Laboratory of Electric Drive and Control of Anhui Higher Education Institutes(DQKJ202006), the Crosswise Project of West Anhui University in 2020 "Intelligent production line of metal composite board (sub-project)"(20201203), Crosswise Project of West Anhui University in 2021 "Intelligent upgrade of high-speed turning center unit components"(20210330), Key Project of Natural Science Research in Universities of Anhui Province(KJ2021A0947), Key project of Natural Science Research in West Anhui University (WXZR202116).

References

[1] WU, C.S., TSAI, P.H., KUO, C.M., TSAI, C.W., (2018). Effect of Atomic Size Difference on the Microstructure and Mechanical Properties of High-Entropy Alloys. *ENTROPY*, Vol. 20, No. 12, pp. https://doi.org/10.3390/e20120967

[2] HUANG, Y., YEH, J.W., YANG, A.C.M., (2021). "High-entropy polymers": A new route of polymer mixing with suppressed phase separation. *MATERIALIA*, Vol. 15, No. pp. https://doi.org/10.1016/j.mtla.2020.100978

[3] LIN, P.T., WU, C.S., PENG, C.H., TSAI, C.W., SATO, Y.S., (2020). Effects of rotational speed on the $Al_{0.3}CoCrCu_{0.3}FeNi$ high-entropy alloy by friction stir welding. *HIGH TEMPERATURE MATERIALS AND PROCESSES*, Vol. 39, No. pp. 556-566. https://doi.org/10.1515/htmp-2020-0046

[4] PENG, C.H., TSAI, C.W., KUO, C.M., CHIU, S.M., (2022). High-Temperature Tribological Behavior of $Al_{0.3}Cr_{0.5}Fe_{1.5}Mn_{0.5}Ni$ High-Entropy Alloys with Addition of Titanium and Carbon. *FRONTIERS IN MATERIALS*, Vol. 8, No. pp. https://doi.org/10.3389/fmats.2021.787729

[5] PRUSA, F., KRATOCHVíL, P., THÜRLOVÁ, H., RUDOMILOVA, D., MSALLAMOVÁ, S., (2023). Influence of the Mn Content on the Corrosion Behaviour of HEA CoCrFeNiMnX (X=5, 20, 35 at.%) Prepared via MA+SPS. *MANUFACTURING TECHNOLOGY*, Vol. 23, No. 2, pp. 247-253. https://doi.org/10.21062/mft.2023.016

[6] SHEN, J.S., LEI, S., FANG, J.G., LIU, Y.F., HU, Z.Q., CUI, S.J., ZHANG, H.L., XUE, Z.W., (2023). Effect of High Temperature Heat Treatment on the Structure and Properties of FeCoCrNiZr Alloy. *Manufacturing technology*, Vol. 23, No. 3, pp. 326-332. https://doi.org/10.21062/mft.2023.041

[7] YEH, J.W., CHEN, S.K., LIN, S.J., GAN, J.Y., CHIN, T.S., SHUN, T.T., TSAU, C.H., CHANG, S.Y., (2004). Nanostructured high-entropy alloys with multiple principal elements: novel alloy design concepts and outcomes. *Advanced engineering materials*, Vol. 6, No. 5, pp. 299-303. https://doi.org/https://doi.org/10.1002/adem.200300567

[8] ZHANG, Z., ZHANG, J., ZHANG, M., PENG, P., (2022). First-principles calculations

on brazed diamond with FeCoCrNi high entropy alloys doped with strong carbide-forming elements. *Solid State Communications*, Vol. 357, No. pp. 114980. https://doi.org/https://doi.org/10.1016/j.ssc.2022.114980

[9] YU, Y., YU, Y., (2022). Simulations of irradiation resistance and mechanical properties under irradiation of high-entropy alloy NiCoCrFe. *Materials Today Communications*, Vol. 33, No. pp. 104308. https://doi.org/https://doi.org/10.1016/j.mtcomm.2022.104308

[10] ALI, M.M., ABD ELMOAMEN, S.S., GEPREEL, M.A.H., AHMED, H.A., ELREFAIE, F.A., (2021). High temperature oxidation of non equi-atomic Al5Cr12Fe35Mn28Ni20 high entropy alloy. *Materials Research Express*, Vol. 8, No. 3, pp. https://doi.org/10.1088/2053-1591/abeab9

[11] ZHANG, C., ZHAO, Z., LIN, X., WANG, S., WANG, J., LI, Y., LI, Y., ZHANG, Y., ZHAO, H., (2024). Molybdenum-14Rhenium Alloy—The Most Promising Candidate for High-Temperature Semiconductor Substrate Materials. *Journal of Alloys and Compounds*, Vol. No. pp. 174391. https://doi.org/https://doi.org/10.1016/j.jallcom.2024.174391

[12] ZHU, Z.X., LIU, X.B., LIU, Y.F., ZHANG, S.Y., MENG, Y., ZHOU, H.B., ZHANG, S.H., (2023). Effects of Cu/Si on the microstructure and tribological properties of FeCoCrNi high entropy alloy coating by laser cladding. *WEAR*, Vol. 512, No. pp. https://doi.org/10.1016/j.wear.2022.204533

[13] ZHOU, Z., LI, H., LIU, Y., NIU, T., LI, H., (2022). Effect of Ti on the corrosion behavior of (FeCrCoNi)100−xTix alloy. *Corrosion Science*, Vol. 209, No. pp. 110807. https://doi.org/https://doi.org/10.1016/j.corsci.2022.110807

[14] ZHANG, X., LIU, L., YAO, K.D., DUAN, K., WU, F.F., ZHAO, R.D., ZHANG, Y., SHANG, J., CHEN, M.H., (2022). The evolution of eutectic microstructure and mechanical properties of AlxCoCrFeNi2.1 high-entropy alloys. *JOURNAL OF MATERIALS RESEARCH*, Vol. 37, No. 12, pp. 2082-2092. https://doi.org/10.1557/s43578-022-00620-3

[15] WAN, Q., HUA, K., ZHOU, Z., ZHANG, F., WU, H., ZHOU, Q., WANG, H., (2023). Revealing the B addition on tribology performance in TiZrHfTa0.5 refractory high-entropy alloy at ambient and elevated temperature. *Journal of Alloys and Compounds*, Vol. 931, No. pp. 167521. https://doi.org/https://doi.org/10.1016/j.jallcom.2022.167521

[16] XU, T., CHEN, Q.J., JI, L., ZHENG, Z.D., WANG, K., LIU, H.Y., (2023). BCC/B2 structure and dislocation strengthening behavior in high Ti content TiAlVCrNb high-entropy alloys. *JOURNAL OF ALLOYS AND COMPOUNDS*, Vol. 956, No. pp. https://doi.org/10.1016/j.jallcom.2023.170179

[17] ZHANG, Y.P., CHEN, X.Z., JAYALAKSHMI, S., SINGH, R.A., DEEV, V.B., PRUSOV, E.S., (2021). Factors determining solid solution phase formation and stability in CoCrFeNiX0.4 (X=Al, Nb, Ta) high entropy alloys fabricated by powder plasma arc additive manufacturing. *JOURNAL OF ALLOYS AND COMPOUNDS*, Vol. 857, No. pp. https://doi.org/10.1016/j.jallcom.2020.157625

[18] STRAKOSOVA, A., KRATOCHVíL, P., RIEDL, J., PRUSA, F., (2022). Phase and Mechanical Properties Response of the Mechanically Alloyed CoCrFeNiAlX High Entropy Alloys. *Manufacturing technology*, Vol. 22, No. 4, pp. 471-476. https://doi.org/10.21062/mft.2022.059

[19] XIA, S.Q., XIA, Z.X., ZHAO, D., XIE, Y., LIU, X., WANG, L., (2021). Microstructure formation mechanism and corrosion behavior of FeCrCuTiV two-phase high entropy alloy prepared by different processes. *FUSION ENGINEERING AND DESIGN*, Vol. 172, No. pp. https://doi.org/10.1016/j.fusengdes.2021.112792

[20] LI, H.Y., ZHANG, Y.J., DESTECH PUBLICAT, I. Effect of Ti Content on Microstructure and Properties on AlCrCoFeNiTi$_x$ High Entropy Alloys. In 2016 INTERNATIONAL CONFERENCE ON MATERIALS SCIENCE AND ENGINEERING APPLICATION (ICMSEA 2016), 2016.

[21] CAO, Y.K., LIU, Y., LIU, B., ZHANG, W.D., (2018). Precipitation behavior during hot deformation of powder metallurgy Ti-Nb-Ta-Zr-Al high entropy alloys. *INTERMETALLICS*, Vol. 100, No. pp. 95-103. https://doi.org/10.1016/j.intermet.2018.06.007

[22] EISSMANN, N., KLöDEN, B., WEISSGäRBER, T., KIEBACK, B., (2017). High-entropy alloy CoCrFeMnNi produced by powder metallurgy. *POWDER METALLURGY*, Vol. 60, No. 3, pp. 184-197. https://doi.org/10.1080/00325899.2017.1318480

[23] GLUDOVATZ, B., HOHENWARTER, A., CATOOR, D., CHANG, E.H., GEORGE, E.P., RITCHIE, R.O., (2014). A fracture-resistant high-entropy alloy for cryogenic applications. Vol. 345, No. 6201, pp. 1153-1158. https://doi.org/doi:10.1126/science.1254581

[24] DENG, Y., TASAN, C.C., PRADEEP, K.G., SPRINGER, H., KOSTKA, A., RAABE, D., (2015). Design of a twinning-induced plasticity high entropy alloy. *Acta Materialia*, Vol. 94, No. pp. 124-133. https://doi.org/https://doi.org/10.1016/j.actamat.2015.04.014

[25] A, A.M., A, S.S., B, S.H., B, N.F.J.J.O.A., COMPOUNDS, (2016). Heat treatment impacts the micro-structure and mechanical properties of AlCoCrFeNi high entropy alloy. Vol. 683, No. pp. 221-230.

[26] SCHNEIDER, M., GEORGE, E.P., MANESCAU, T.J., ZÁLEZÁK, T., HUNFELD, J., DLOUHY, A., EGGELER, G., LAPLANCHE, G., (2020). Analysis of strengthening due to grain boundaries and annealing twin boundaries in the CrCoNi medium-entropy alloy. *INTERNATIONAL JOURNAL OF PLASTICITY*, Vol. 124, No. pp. 155-169. https://doi.org/10.1016/j.ijplas.2019.08.009

[27] ZHAO, Y.Y., CHEN, H.W., LU, Z.P., NIEH, T.G., (2018). Thermal stability and coarsening of coherent particles in a precipitation-hardened $(NiCoFeCr)_{94}Ti_2Al_4$ high-entropy alloy. *ACTA MATERIALIA*, Vol. 147, No. pp. 184-194. https://doi.org/10.1016/j.actamat.2018.01.049

[28] MA, Y., WANG, Q., JIANG, B.B., LI, C.L., HAO, J.M., LI, X.N., DONG, C., NIEH, T.G., (2018). Controlled formation of coherent cuboidal nanoprecipitates in body-centered cubic high-entropy alloys based on $Al_2(Ni,Co,Fe,Cr)_{14}$ compositions. *ACTA MATERIALIA*, Vol. 147, No. pp. 213-225. https://doi.org/10.1016/j.actamat.2018.01.050

[29] SLONE, C.E., MIAO, J., GEORGE, E.P., MILLS, M.J., (2019). Achieving ultra-high strength and ductility in equiatomic CrCoNi with partially recrystallized microstructures. *ACTA MATERIALIA*, Vol. 165, No. pp. 496-507. https://doi.org/10.1016/j.actamat.2018.12.015

[30] XIAO, J.K., TAN, H., CHEN, J., MARTINI, A., ZHANG, C., (2020). Effect of carbon content on microstructure, hardness and wear resistance of $CoCrFeMnNiC_x$ high-entropy alloys. *JOURNAL OF ALLOYS AND COMPOUNDS*, Vol. 847, No. pp. https://doi.org/10.1016/j.jallcom.2020.156533

[31] HE, M.W., EIZADJOU, M., CHEN, H.S., LIU, H.W., CHANG, L., RINGER, S.P., (2022). Microstructure and properties of CoCrFeN based multi-principal element alloys containing C and Sc. *JOURNAL OF MATERIALS SCIENCE*, Vol. 57, No. 20, pp. 9442-9453. https://doi.org/10.1007/s10853-022-07227-3

[32] SEKHAR, R.A., SHIFIN, A.S., FIROZ, N., (2021). Microstructure and mechanical properties of AlCoCrNiTi-C High Entropy Alloy processed through Spark Plasma Sintering. *MATERIALS CHEMISTRY AND PHYSICS*, Vol. 270, No. pp. https://doi.org/10.1016/j.matchemphys.2021.124846

[33] LIN, C.M., TSAI, H.L., BOR, H.Y., (2010). Effect of aging treatment on microstructure and properties of high-entropy $Cu_{0.5}CoCrFeNi$ alloy. *INTERMETALLICS*, Vol. 18, No. 6, pp. 1244-1250. https://doi.org/10.1016/j.intermet.2010.03.030

[34] XU, Z.Q., MA, Z.L., TAN, Y., WANG, M., ZHAO, Y., CHENG, X.W.J.J.O.A., SCIENCE, C.A.I.J.O.M., CHEMISTRY, S.-S., PHYSICS, (2022). Effects of Si additions on microstructures and mechanical properties of VNbTiTaSix refractory high-entropy alloys. Vol. No. 900-, pp. 900.

[35] XIN, J.M., JUNHU %J JOURNAL OF ALLOYS, SCIENCE, C.A.I.J.O.M., CHEMISTRY, S.-S., PHYSICS, (2021). Improving mechanical properties and tribological performance of Al0.2Co1.5CrFeNi1.5Ti0.5 high entropy alloys via doping Si. Vol. 869, No. 1, pp.

[36] LI, Y.Z., SHI, Y., OLUGBADE, E., (2020). Microstructure, mechanical, and corrosion resistance properties of $Al_{0.8}CrFeCoNiCu_x$ high-entropy alloy coatings on aluminum by laser cladding. *MATERIALS RESEARCH*

EXPRESS, Vol. 7, No. 2, pp. https://doi.org/10.1088/2053-1591/ab6c9b

[37] LI, Y.Z., SHI, Y., (2021). Microhardness, wear resistance, and corrosion resistance of AlxCrFeCoNiCu high-entropy alloy coatings on aluminum by laser cladding. *OPTICS AND LASER TECHNOLOGY*, Vol. 134, No. pp. https://doi.org/10.1016/j.optlastec.2020.106632

[38] LU, Y.P., DONG, Y., JIANG, H., WANG, Z.J., CAO, Z.Q., GUO, S., WANG, T.M., LI, T.J., LIAW, P.K., (2020). Promising properties and future trend of eutectic high entropy alloys. *SCRIPTA MATERIALIA*, Vol. 187, No. pp. 202-209. https://doi.org/10.1016/j.scriptamat.2020.06.022

[39] LI, Y., WANG, X., SHI, Z., LIANG, J., (2023). Phase Structure, Microstructure, Corrosion, and Wear Resistance of Al0.8CrFeCoNiCu0.5 High-Entropy Alloy. Vol. 11, No. 9, pp. 358.

[40] ZHANG, Y., CHEN, Z., CAO, D.D., ZHANG, J.Y., ZHANG, P., TAO, Q., YANG, X.Q., (2019). Concurrence of spinodal decomposition and nano-phase precipitation in a multi-component AlCoCrCuFeNi high-entropy alloy. *JOURNAL OF MATERIALS RESEARCH AND TECHNOLOGY-JMR&T*, Vol. 8, No. 1, pp. 726-736. https://doi.org/10.1016/j.jmrt.2018.04.020

[41] ROCHE, V., CHAMPION, Y., BATAEV, I.A., JORGE, A.M., (2022). Passive film formation on the new biocompatible non-equiatomic Ti21Nb24Mo23Hf17Ta15 high entropy alloy before and after resting in simulated body fluid. *CORROSION SCIENCE*, Vol. 207, No. pp. https://doi.org/10.1016/j.corsci.2022.110607

[42] LU, C.W., LU, Y.S., LAI, Z.H., YEN, H.W., LEE, Y.L., (2020). Comparative corrosion behavior of $Fe_{50}Mn_{30}Co_{10}Cr_{10}$ dual-phase high-entropy alloy and CoCrFeMnNi high-entropy alloy in 3.5 wt% NaCl solution. *JOURNAL OF ALLOYS AND COMPOUNDS*, Vol. 842, No. pp. https://doi.org/10.1016/j.jallcom.2020.155824

[43] LEE, C.P., CHEN, Y.Y., HSU, C.Y., YEH, J.W., SHIH, H.C., (2008). Enhancing pitting corrosion resistance of Al x CrFe 1.5MnNi 0.5 high-entropy alloys by anodic treatment in sulfuric acid. *THIN SOLID FILMS*, Vol. 517, No. 3, pp. 1301-1305. https://doi.org/10.1016/j.tsf.2008.06.014

[44] ZHAO, R.F., REN, B., CAI, B., LIU, Z.X., ZHANG, G.P., ZHANG, J.J., (2019). Corrosion behavior of Co_x CrCuFeMnNi high-entropy alloys prepared by hot pressing sintered in 3.5% NaCl solution. *RESULTS IN PHYSICS*, Vol. 15, No. pp. https://doi.org/10.1016/j.rinp.2019.102667

[45] ZHANG, Z.J., YUAN, T.C., LI, R.D., (2020). Striped Non-Uniform Corrosion Behavior of Non-Equiatomic FeMnCoCr High-Entropy Alloy Prepared by Laser Melting Deposition in 0.1 M H_2SO_4 Solution. *MATERIALS*, Vol. 13, No. 23, pp. https://doi.org/10.3390/ma13235554

[46] LI, Z.Z., ZHAO, S.T., RITCHIE, R.O., MEYERS, M.A., (2019). Mechanical properties of high-entropy alloys with emphasis on face-centered cubic alloys. *PROGRESS IN MATERIALS SCIENCE*, Vol. 102, No. pp. 296-345. https://doi.org/10.1016/j.pmatsci.2018.12.003

[47] VERMA, A., TARATE, P., ABHYANKAR, A.C., MOHAPE, M.R., GOWTAM, D.S., DESHMUKH, V.P., SHANMUGASUNDARAM, T., (2019). High temperature wear in $CoCrFeNiCu_x$ high entropy alloys: The role of Cu. *SCRIPTA MATERIALIA*, Vol. 161, No. pp. 28-31. https://doi.org/10.1016/j.scriptamat.2018.10.007